PNAS
www.pnas.org

Supplementary Information for:

Peroxidasin-mediated bromine enrichment of basement membranes

Cuiwen He*, Wenxin Song*, Thomas A. Weston, Caitlyn Tran, Ira Kurtz, Jonathan E. Zuckerman, Paul Guagliardo, Jeffrey H. Miner, Sergey V. Ivanov, Jeremy Bougoure, Billy G. Hudson, Selene Colon, Paul A. Voziyan, Gautam Bhave, Loren G. Fong, Stephen G. Young*, and Haibo Jiang*

*Cuiwen He and Wenxin Song wish to be identified as co-first authors; Stephen Young and Haibo Jiang wish to be considered co-senior authors.

Correspondence: Stephen G. Young, 675 Charles E. Young Dr. South, Los Angeles, CA 90095. Tel: (310) 825-4934; Fax: (310) 206-0865; E-mail: sgyoung@mednet.ucla.edu or Haibo Jiang, 35 Stirling Highway, Perth 6009, Australia; Tel: +61864887056; E-mail: haibo.jiang@uwa.edu.au

This PDF file includes: Supplementary *Materials and Methods,* Figures S1–S12, and Table S1

Supplementary Materials and Methods

Further information on *Pxdn*-deficient mouse strains. The peroxidasin knockout mice described by Yan *et al*. (1) exhibited dysgenesis of the anterior chamber of the eye but were free of obvious renal pathology. The same findings were observed in the $Pxdn^{-/-}$ mice generated by Bhave *et al.* (2). Bhave *et al*. (2) had reported that the levels of collagen IV sulfilimine crosslinks in kidneys of $Pxdn^{-/-}$ mice were ~30% of those in wild-type mice. Subsequently, Sirokmany *et al.* (3) analyzed an independent line of peroxidasin knockout mice harboring a frameshift mutation near the beginning of the peroxidasin domain coding sequences and observed a virtual absence of sulfilimine bonds. The persistence of 30%-normal levels of sulfilimine crosslinks in the $Pxdn^{-/-}$ mice generated by Bhave *et al*. (2), which had been generated with a gene-trap allele, raised the possibility that the gene-trap allele was "leaky" (*i.e.,* that there was splicing around the insertional mutation, allowing for expression of low levels of peroxidasin transcripts). Later, Bhave and coworkers used *Cre* recombinase to excise exon 9 from their gene-trap *Pxdn* knockout allele. No homozygous mice lacking exon 9 were born, adding to suspicions that the parental gene-trap allele was "leaky." Because our goal was to analyze tissues of adult mice, our study utilized the original gene-trap $Pxdn^{-/-}$ mice created by Bhave *et al*. (2).

Quantifying Pxdn transcripts by RT-PCR. To test whether low levels of *Pxdn* transcripts were produced by the gene-trap $Pxdn^{-/-}$ mice, total RNA was isolated from wild-type and $Pxdn^{-/-}$ mice with an RNeasy Mini Kit (Qiagen). RNA yield and purity were quantified by Nanodrop spectrophotometric measurement at 260 nm (Thermo Fisher). cDNA was reverse-transcribed from 5 μg total RNA with oligo$(dT)_{20}$ primer and SuperScript III Reverse Transcriptase (Invitrogen Life Technologies). qRT-PCR was performed using PowerUp SYBR Green Master Mix (Applied Biosystems, Thermo Fisher Scientific) in a CFX96 Real-Time System (Bio-Rad, Hercules, CA) using a reaction volume of 20 μl for 40 cycles. The mouse *Pxdn* primers were designed to create an amplicon spanning exons 8 and 9 (Forward, 5′–CTCAGGGAACACAGTGTACTT–3′ and Reverse 5′–TCCGTCTTCATGCTCAACTC–3′). Samples were run in triplicate and mean C_q (quantification cycle) values determined. *Pxdn* transcript levels were calculated relative to housekeeping genes *Hprt* and *B2m*.

NanoSIMS instrument settings. For Fig. 2 and Fig. 3, 30 × 30-μm regions were scanned with a primary ion beam current of ∼1.2-nA (primary aperture D1=1) to reach a dose of ∼1 × 10^{17} ions/cm^2 (thereby removing the gold coating and implanting $^{133}Cs^+$ to ensure a steady state of secondary ion release). Regions of 28 × 28-μm were imaged with an 8-pA beam current (primary aperture D1=2) and a total dwell time of 15 ms/pixel. 512 × 512-pixel images were obtained. For Fig. 4, Fig. 5, Fig. S4, and Fig. S5, samples were scanned with a ∼3-nA beam current (primary aperture D1=1) and a raster of 50 × 50 μm to reach a dose of ∼1 × 10^{17} ions/cm^2. Images were taken with a 4-pA beam current (primary aperture D1=2), a raster of 45 × 45 μm, and a dwell time of 70 ms/pixel. 256 × 256–pixel images were obtained. For Fig. 6, Fig. S6, Fig. S7, Fig. S8, and Fig. S9, samples were scanned with a ∼1-nA beam current (primary aperture D1=1) and a raster of 50 × 50 μm to reach a dose of ∼1 × 10^{17} ions/cm^2. Images were taken with an 8-pA beam current (primary aperture D1=2), a raster of 45 × 45 μm, and a dwell time of 32.5 ms/pixel. 256 × 256–pixel images were obtained. For Fig. 7 and Fig. S11, 30 × 30-μm regions were scanned with a primary ion beam current of ∼1.2-nA (primary aperture D1=1) to reach a dose of ∼1 × 10^{17} ions/cm^2. Regions of 28 × 28-μm were imaged with an 8-pA beam current (primary aperture D1=2) and a total dwell time of 36 ms/pixel. 256 × 256–pixel images were obtained. For Fig. S1, Fig. S2, and Fig. S3 of the *SI Appendix*, 35 × 35-μm regions of the section were scanned with a primary ion beam current of ∼1.2-nA (primary aperture D1=1) to reach a dose of ∼1 × 10^{17} ions/cm^2. Regions of 28 × 28-μm (Fig. S1 and Fig. S2 of the *SI Appendix*) or 30 × 30-μm (Fig. S3 of the *SI Appendix*) were imaged with a 4-pA beam current (primary aperture D1=3) and a total dwell time of 50 ms/pixel. 256 × 256–pixel images were obtained.

Sample preparations and MS^2 spectra generation for LC–MS/MS analysis of bromination sites. Samples were precipitated with 25% trichloroacetic acid on ice for 1 h; after centrifugation at 14,000 × *g*, pellets were washed with cold acetone, dried by Speed-Vac centrifugation, and reconstituted in 50 mM Tris buffer, pH 8, containing 50% trifluoroethanol (TFE). Samples were then treated with Tris(2-carboxyethyl)phosphine to reduce disulfide bonds. Cysteines were carbamidomethylated with iodoacetamide, and the samples were diluted fivefold in 100 mM Tris to obtain a final 10% TFE solution. Samples were then digested with trypsin overnight at 37°C, followed by acidification and dilution with 0.1% formic acid. The resulting peptides from each sample were then loaded onto a capillary reverse-

phase analytical column using an Eksigent NanoLC HPLC with an autosampler. The analytical column was packed with C18 reverse-phase resin (Jupiter, 3-μm beads, 300 Å; Phenomenex). Peptides were gradient-eluted at a flow rate of 500 nl/min; the mobile-phase solvents consisted of 0.1% formic acid, 99.9% water (solvent A) and 0.1% formic acid, 99.9% acetonitrile (solvent B). A 90-min gradient was performed as follows: 0–15 min, 2% B (loading phase); 15–55 min, 2–40% B; 55–65 min, 40–90% B; 65–68 min, 90% B; 68–70 min, 90–2% B; 70–90 min, 2% B. Upon gradient elution, peptides were mass analyzed on an LTQ Orbitrap Velos mass spectrometer (Thermo Scientific), equipped with a nano-ESI source, using a data-dependent method with dynamic exclusion. For all analyses, full scan (m/z 300–2000) spectra were acquired with the Orbitrap as the mass analyzer (resolution 60,000). An isolation width of 2 m/z, activation time of 10 ms, and 35% normalized collision energy were used to generate MS^2 spectra.

MS^2 spectra analysis for LC–MS/MS analysis of bromination sites. All tandem mass spectra were converted into DTA files with Scansifter, and the data were searched against corresponding subsets of the UniProtKB protein database. Protein databases were appended with reversed (decoy) protein sequences to facilitate false discovery rate estimates. Database searches were performed with SEQUEST (4), and results were assembled in Scaffold version 4.3.2 (Proteome Software) with minimum filtering criteria of 95% peptide probability and 99% protein probability. Searches were configured to use variable protein residue modifications: carbamidomethylation of cysteine (ΔM = 57.0215); oxidation of methionine (ΔM = 15.9949); and single and double bromination of lysine, histidine, tyrosine, and tryptophan (ΔM = 77.9105 and 155.8210). Sites of modification were validated by manual interpretation of the raw tandem mass spectra with QualBrowser software (Xcalibur 2.2, Thermo Scientific). Accurate mass measurements of the tryptic peptides were used to generate extracted ion chromatograms (XICs). A window of 10 ppm around the theoretical monoisotopic *m/z* values of the observed precursor ions was utilized for making XICs of the unmodified and brominated peptides. Using QualBrowser (Xcalibur 2.2), the integrated area under the curve (AUC) for each XIC peak was determined. The relative abundance of brominated peptides was then calculated as a ratio of the AUC for modified peptide to the summed AUCs for the modified and unmodified peptides.

References for Supplementary Methods

1. X. Yan *et al.*, Peroxidasin is essential for eye development in the mouse. *Hum Mol Genet* **23**, 5597–5614 (2014).
2. G. Bhave, S. Colon, N. Ferrell, The sulfilimine cross-link of collagen IV contributes to kidney tubular basement membrane stiffness. *Am J Physiol Renal Physiol* **313**, F596–F602 (2017).
3. G. Sirokmany *et al.*, Peroxidasin-mediated crosslinking of collagen IV is independent of NADPH oxidases. *Redox Biol* **16**, 314-321 (2018).
4. J. K. Eng, A. L. Mccormack, J. R. Yates, An approach to correlate tandem mass-spectral data of peptides with amino-acid-sequences in a protein database. *Journal of the American Society for Mass Spectrometry* **5**, 976–989 (1994).

***SI Appendix,* Figures S1–S12, Table S1**

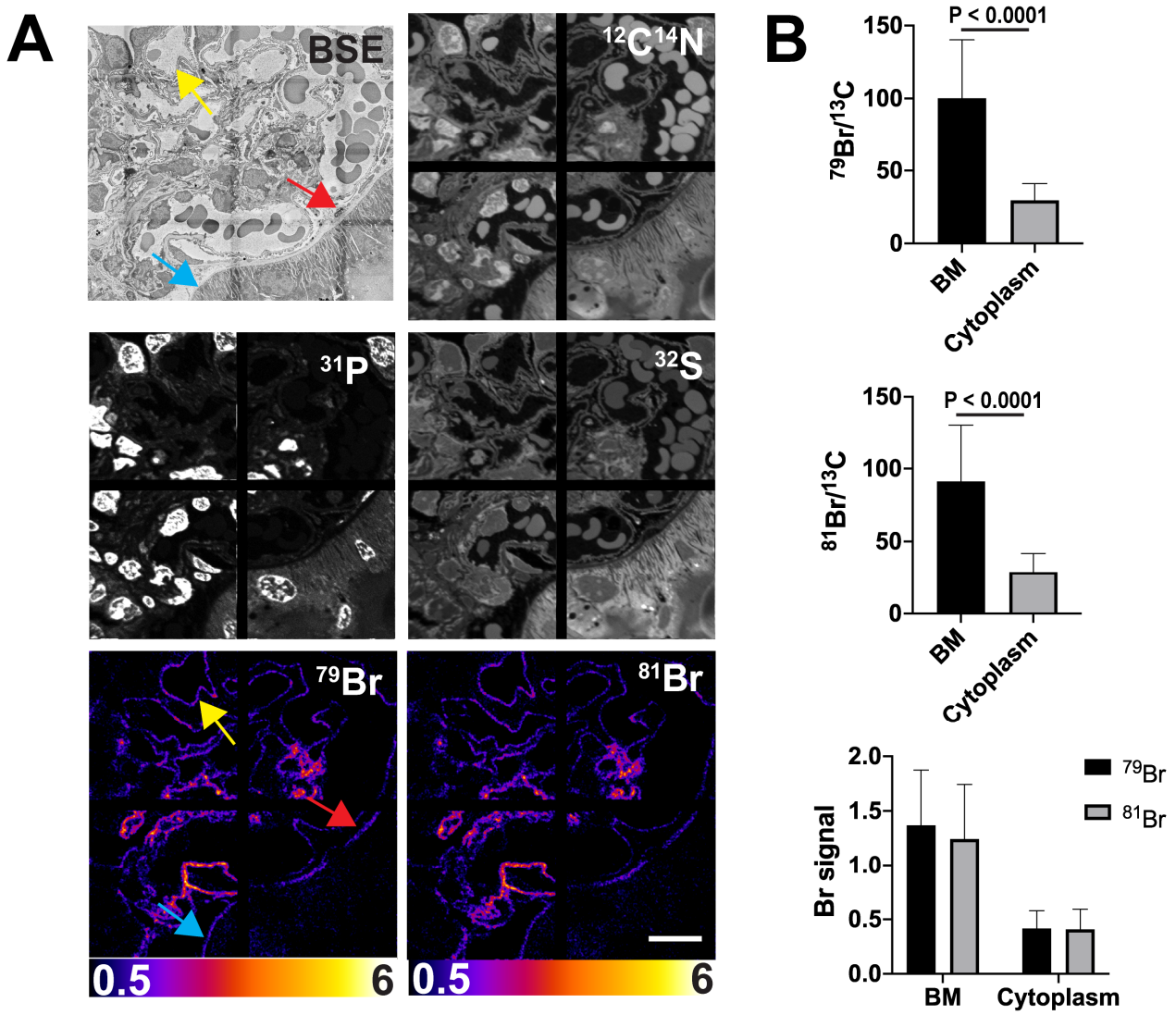

Fig. S1. Bromine (^{79}Br, ^{81}Br) is enriched in basement membranes of mouse kidney, as judged by correlative electron microscopy and NanoSIMS analyses. (A) A glomerulus was mapped by backscattered electron (BSE) imaging and NanoSIMS. ^{31}P, ^{12}C^{14}N, and ^{32}S NanoSIMS images were useful for defining tissue morphology. ^{79}Br and ^{81}Br NanoSIMS images reveal bromine enrichment in the basement membrane. Red arrows, Bowman's capsule; blue arrows, renal tubule; yellow arrows, glomerular capillary. Scale bars, 10 µm. (B) Quantification of ^{79}Br and ^{81}Br (normalized to ^{13}C) for regions of interest (ROI) (mean ± SD) in the basement membrane (BM, n = 110 ROIs) and in the cytoplasm of glomerular endothelial cells and podocytes (n = 93 ROIs). Also shown is a comparison of ^{79}Br and ^{81}Br enrichment in the BM and the glomerular cells. ^{79}Br/^{13}C and ^{81}Br/^{13}C ratios were multiplied by 10,000.

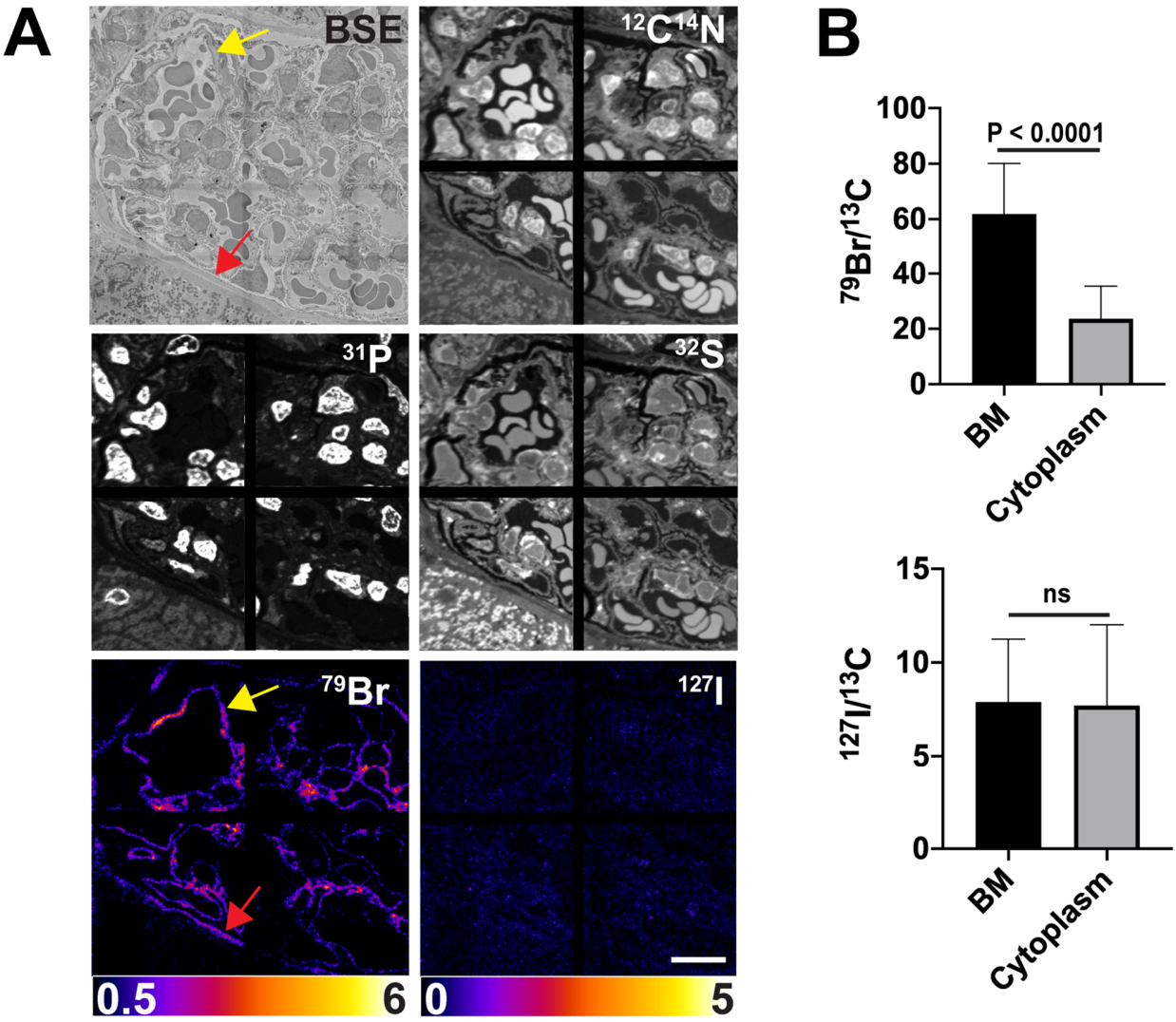

Fig. S2. Basement membranes of mouse kidney are enriched in bromine but not iodine, as judged by correlative backscattered electron imaging (BSE) and NanoSIMS analyses. (A) A glomerulus was mapped by electron microscopy and NanoSIMS. ^{31}P, $^{12}C^{14}N$, and ^{32}S NanoSIMS images were useful for defining tissue morphology. The ^{79}Br NanoSIMS image revealed bromine enrichment in the basement membranes; the ^{127}I NanoSIMS image revealed little or no ^{127}I enrichment in basement membranes of mouse kidney, relative to amounts of ^{127}I within cytoplasm of glomerular cells. Red arrow, Bowman's capsule; yellow arrow, glomerular capillary. Scale bars, 10 µm. (B) Quantification of ^{79}Br and ^{127}I (normalized to ^{13}C) for regions of interest (ROI) (mean ± SD) in basement membranes (BM, n = 105 ROIs) and cytoplasm of glomerular cells (n = 176 ROIs). Ratios were multiplied by 10,000.

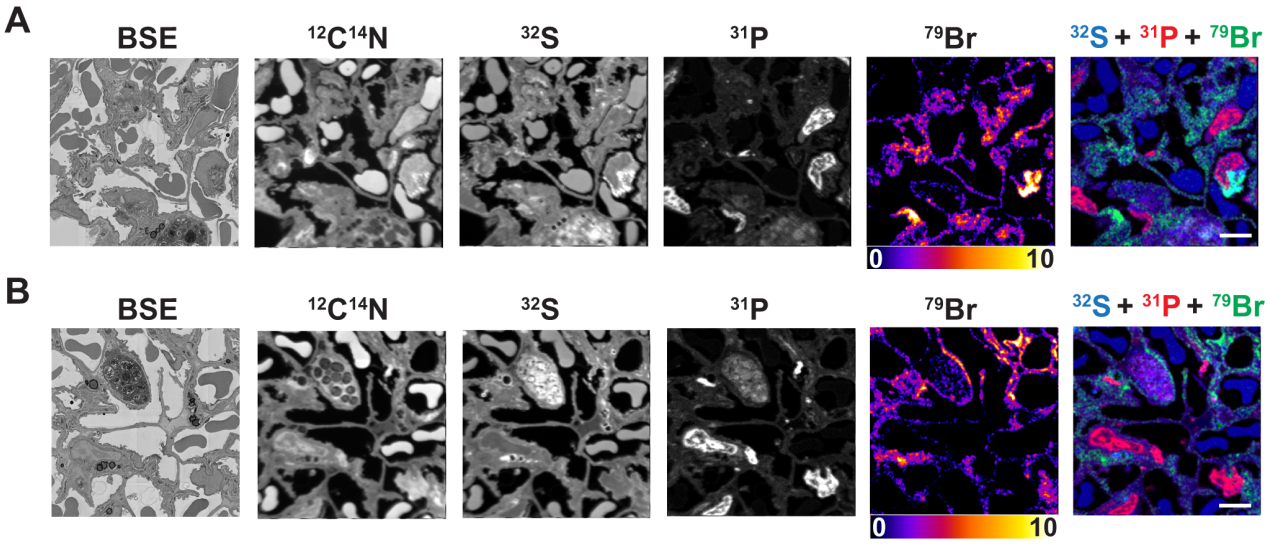

Fig. S3. Bromine is enriched in basement membranes of the mouse lung. Lung tissue (from the same mouse examined in Fig. 1) was collected and processed for backscattered electron (BSE) imaging and NanoSIMS analyses. Panels A and B show two fields of the section. $^{12}C^{14}N$, ^{31}P, and ^{32}S images were useful for visualizing tissue morphology. ^{79}Br images show bromine distribution in the lung. ^{79}Br enrichment was confined to basement membranes (identified by BSE images as well as $^{12}C^{14}N$ and ^{32}S NanoSIMS images). Scale bars, 5 μm.

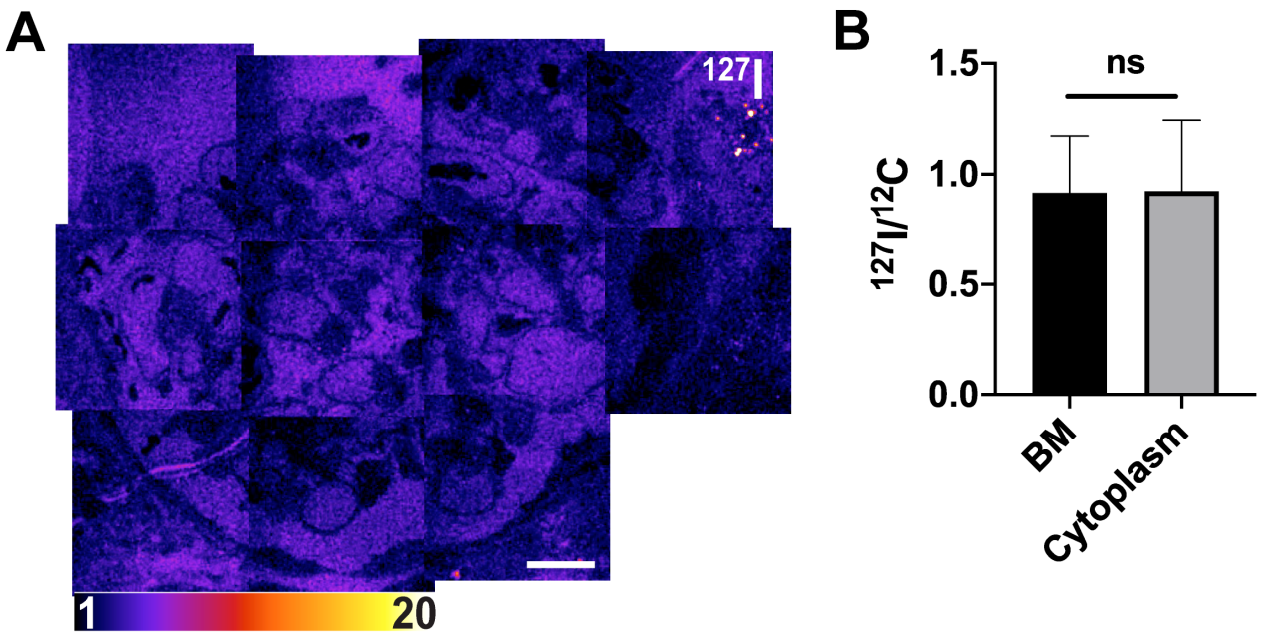

Fig S4. Human kidney basement membranes are not enriched in iodine. (A) ^{127}I NanoSIMS images of the same normal human glomerulus shown in Fig. 4, revealing that ^{127}I is not enriched in basement membranes of the human kidney. Scale bars, 20 μm. (B) Quantification of ^{127}I (normalized to ^{12}C) (mean ± SD) in basement membranes (BM, n = 351 ROIs) and cytoplasm of glomerular cells (n = 274 ROIs). Ratios were multiplied by 10,000. The relatively higher ^{127}I signals in the resin (*e.g.,* note ^{127}I enrichment in the lumen of glomerular capillaries) compared to basement membranes and glomerular cells are likely due to ^{127}I contamination of the resin during sample preparation.

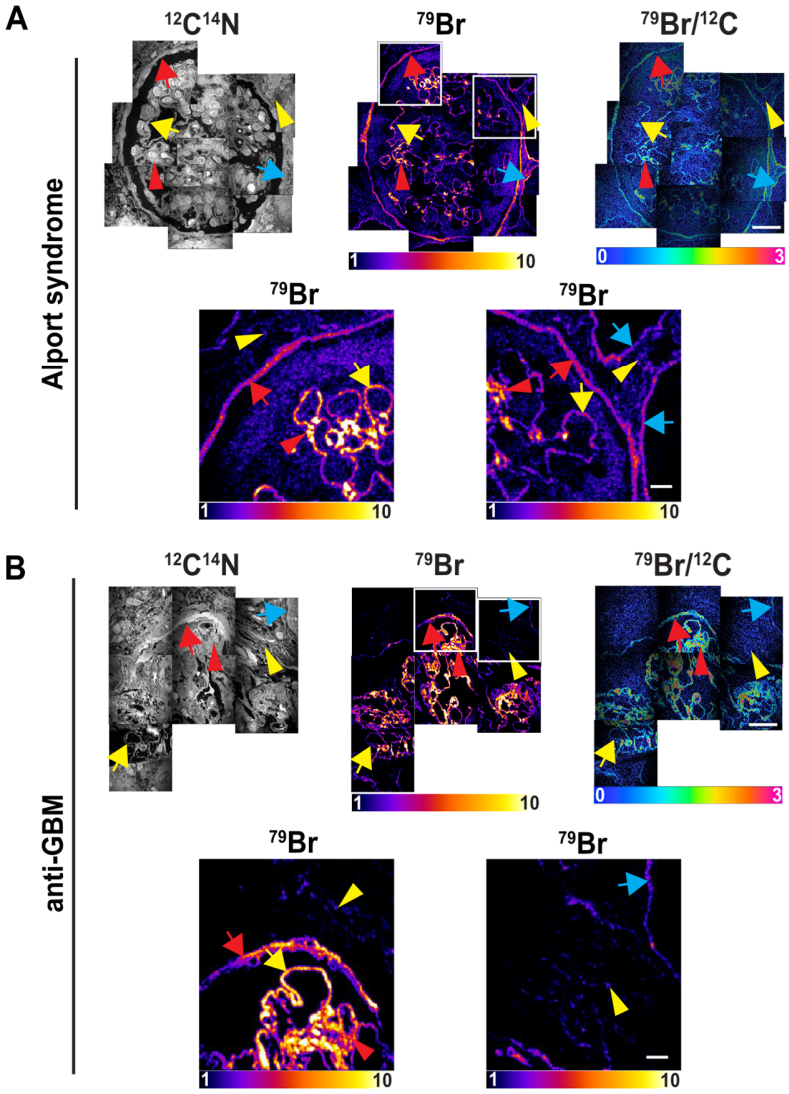

Fig. S5. Bromine enrichment in kidney biopsy specimens from a patient with Alport syndrome (A) and a patient with anti-glomerular basement disease (anti-GBM) (B). $^{12}C^{14}N$ NanoSIMS images were useful for visualizing morphology. ^{79}Br and $^{79}Br/^{12}C$ NanoSIMS images were generated to show bromine distribution and bromine enrichment in the basement membrane of glomerular capillaries (yellow arrows), the basement membrane of renal tubules (blue arrows), the basement membrane of Bowman's capsule (red arrows), the mesangial matrix of the glomerulus (red arrowheads), and the extracellular matrix (yellow arrowheads) between renal tubules. The lower panels of (A) and (B) represent close-up ^{79}Br images of boxed regions in the upper panels. Quantification of the NanoSIMS data for glomerular capillaries in the Alport syndrome specimen revealed a ~35% lower $^{79}Br/^{12}C$ ratio (n = 113 regions of interest) than in two normal kidney specimens analyzed in Fig. 5C (a total 279 regions of interest). The specimen from a patient with anti-GBM disease revealed intense bromine enrichment within the mesangial matrix of the glomerulus (red arrowheads). $^{79}Br/^{12}C$ ratios were multiplied by 10,000. Upper panel scale bars, 20 μm. Lower panel scale bars, 5 μm.

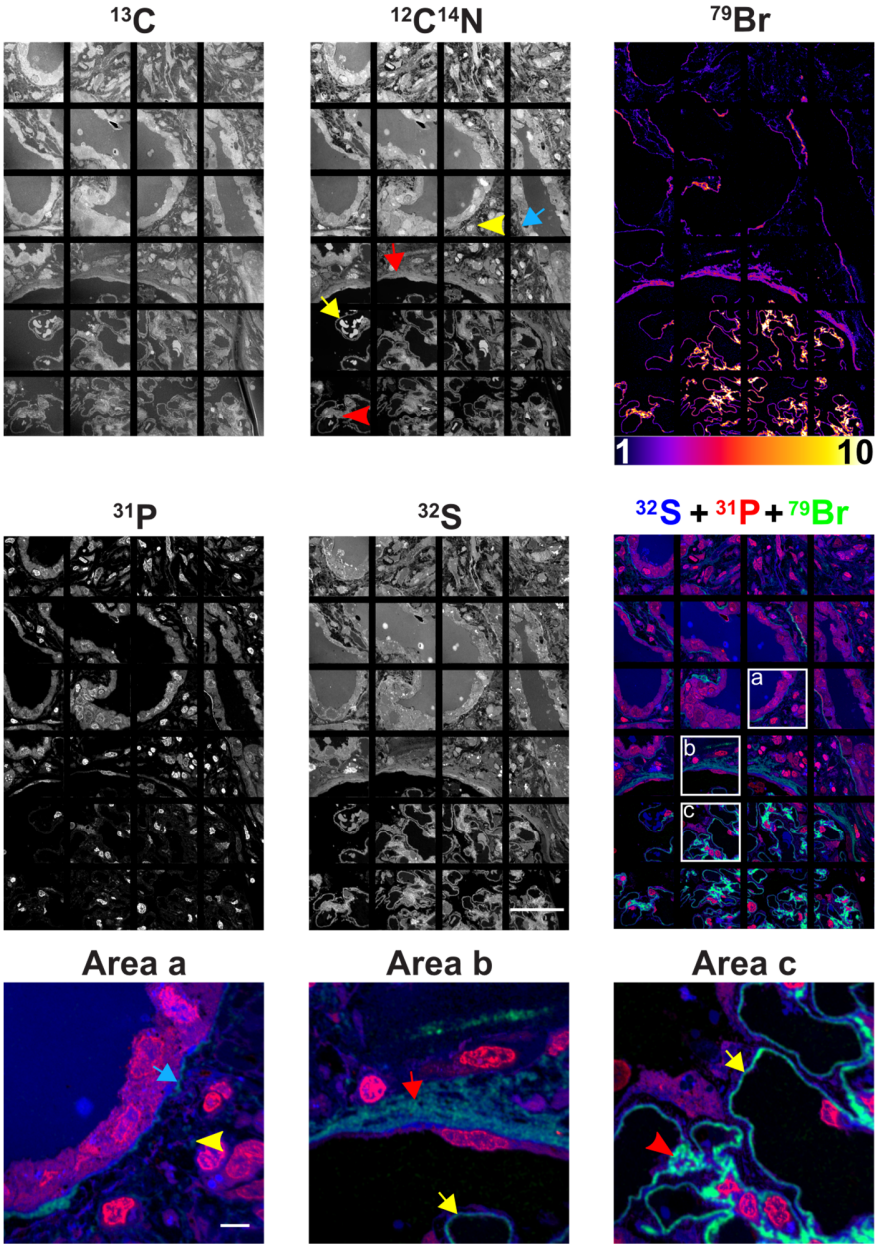

Fig. S6. Bromine enrichment in a kidney biopsy from a patient with eosinophilic interstitial nephritis. ^{13}C, $^{12}C^{14}N$, ^{31}P and ^{32}S NanoSIMS images were useful for visualizing morphology; ^{79}Br and composite ^{31}P (red), ^{32}S (blue), and ^{79}Br (green) NanoSIMS images were generated to show bromine distribution and bromine enrichment in the basement membrane of glomerular capillaries (yellow arrows), the basement membrane of renal tubules (blue arrows), the basement membrane of Bowman's capsule (red arrows), the mesangial matrix of the glomerulus (red arrowheads), and the extracellular matrix (yellow arrowheads) between renal tubules. The lower panels represent close-up composite images of boxed regions (*Area a, Area b, Area c*) in the middle panels. Upper panel and middle panel scale bars, 40 μm. Lower panel scale bars, 5 μm.

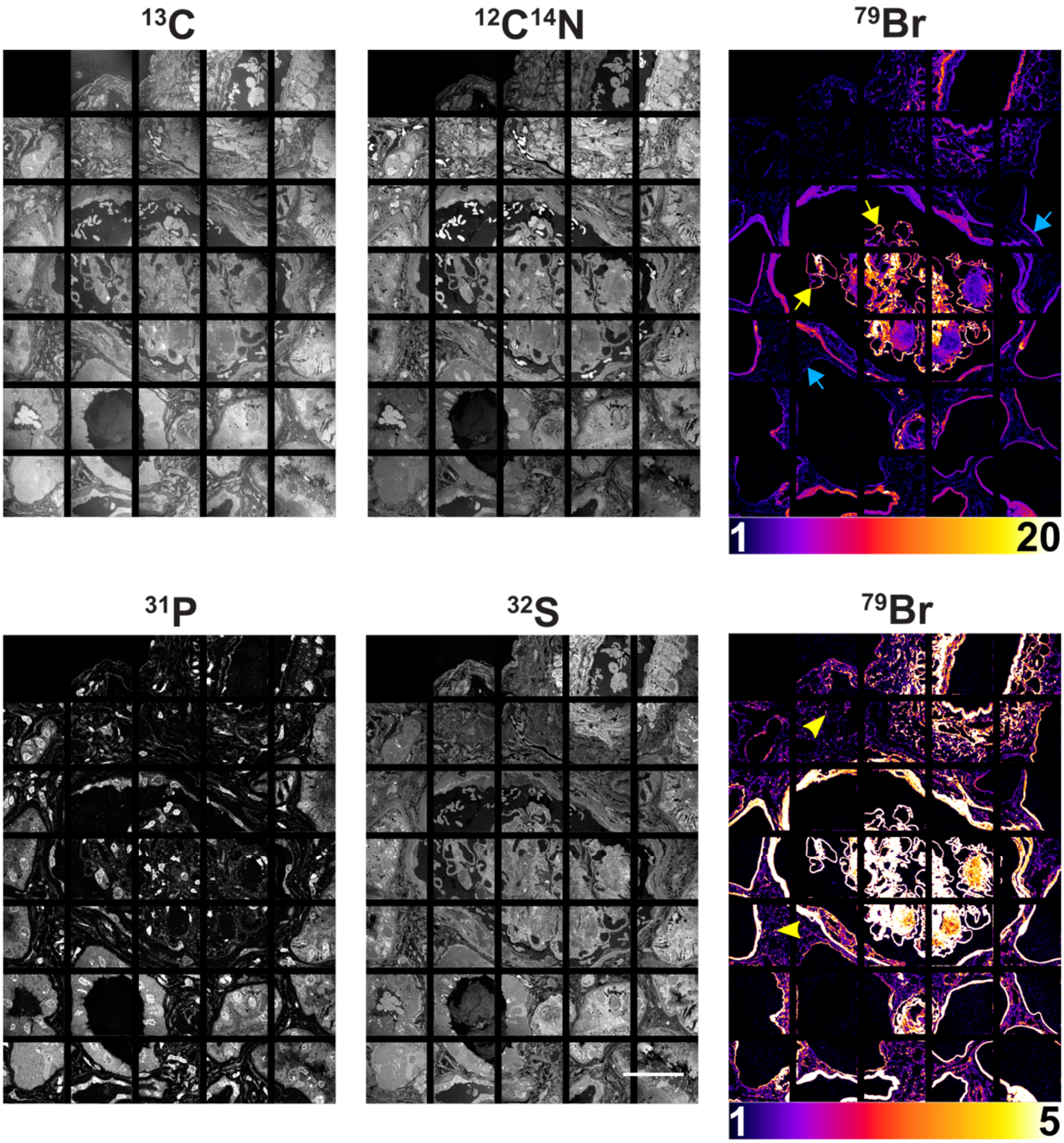

Fig. S7. NanoSIMS images of a kidney biopsy from a patient with diabetic nephropathy. Shown here are ^{13}C, $^{12}C^{14}N$, ^{31}P, ^{32}S and ^{79}Br NanoSIMS images of the kidney biopsy shown in Fig. 6A. ^{79}Br is depicted with two different scales. The 1–5 scale is useful for revealing low levels of ^{79}Br in the extracellular matrix between renal tubules (yellow arrowheads); the 1–20 scale shows that ^{79}Br enrichment in the basement membrane glomerular capillaries (yellow arrows) is greater than in the renal tubule basement membranes (blue arrows). Scale bars, 45 μm.

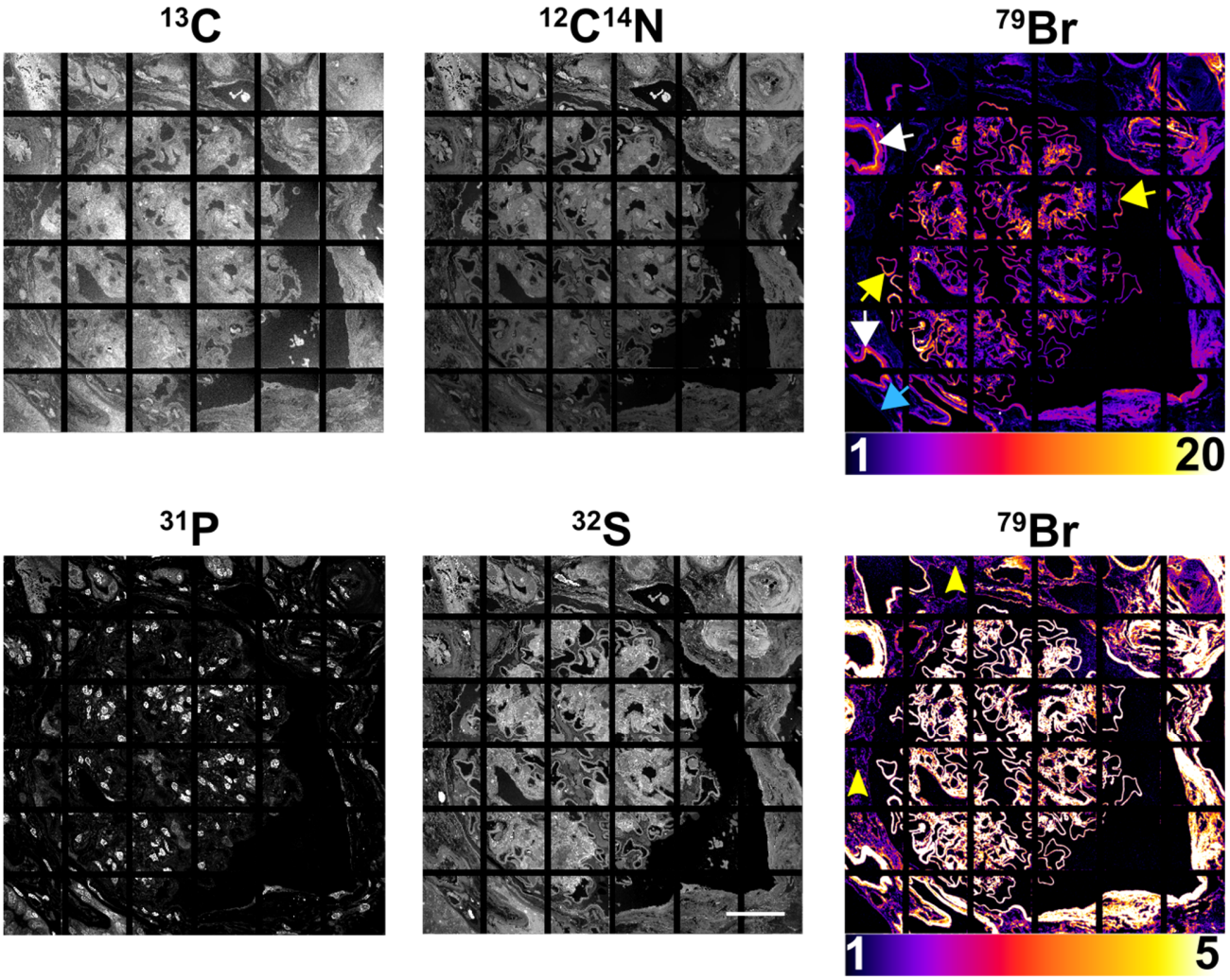

Fig. S8. NanoSIMS images of a kidney biopsy from a patient with diabetic nephropathy. Shown here are ^{13}C, $^{12}C^{14}N$, ^{31}P, ^{32}S, and ^{79}Br NanoSIMS images of the kidney biopsy shown in Fig. 6B. ^{79}Br is depicted with two different scales. The 1–5 scale is useful for showing low levels of ^{79}Br in the extracellular matrix between renal tubules (yellow arrowheads). The 1–20 scale shows that ^{79}Br enrichment in the basement membrane of glomerular capillaries (yellow arrows) is greater than in the renal tubule basement membranes (blue arrow). ^{79}Br enrichment was also high in onion-like basement membranes of atrophic renal tubules (white arrows). Scale bars, 45 μm.

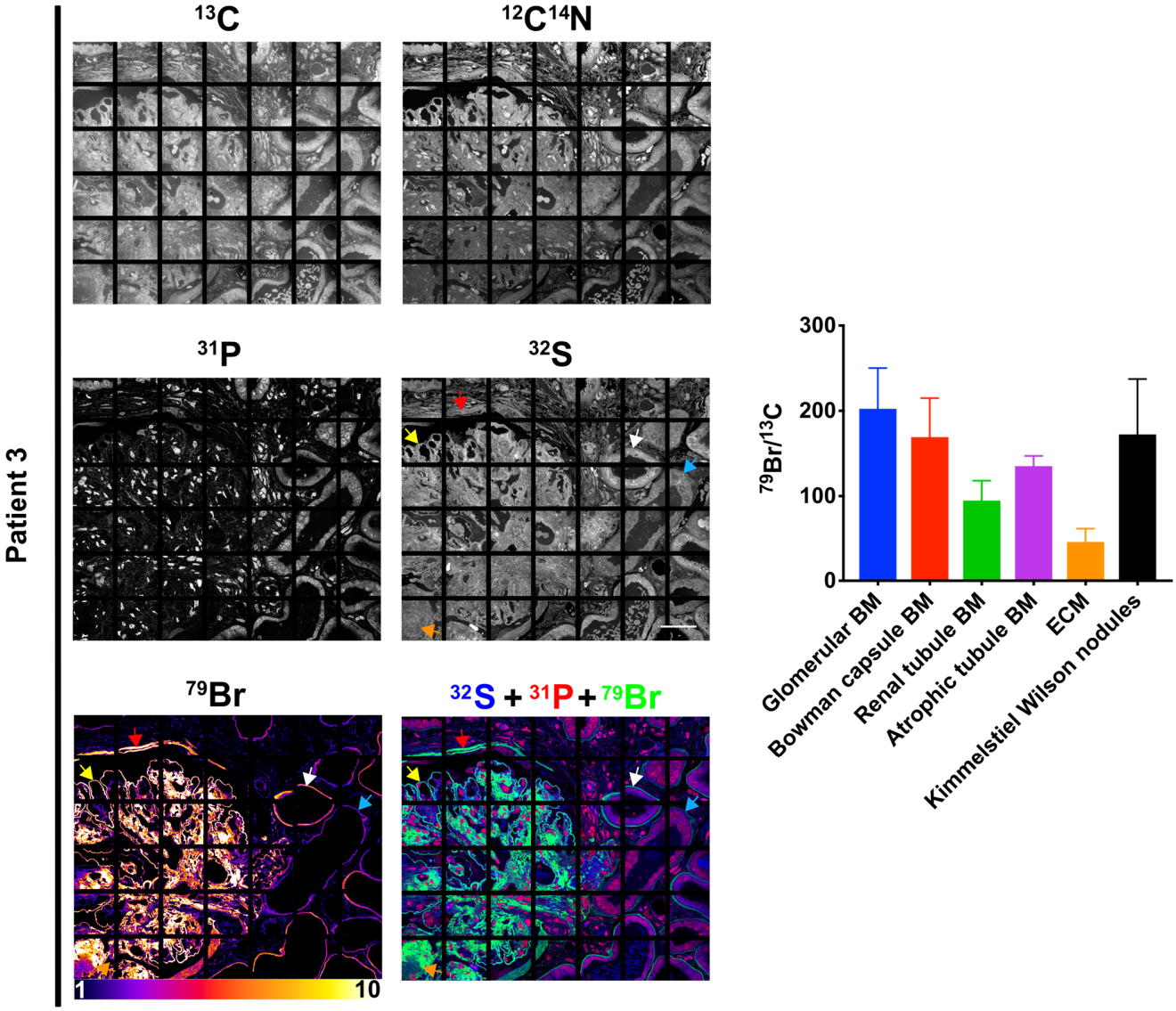

Fig. S9. NanoSIMS images of a kidney biopsy from a patient with diabetic nephropathy. ^{13}C, $^{12}C^{14}N$, ^{31}P, and ^{32}S images were useful for visualizing morphology; the ^{79}Br image and a composite ^{31}P (red), ^{32}S (blue), and ^{79}Br (green) image were generated to show bromine distribution and bromine enrichment in the basement membrane of glomerular capillaries (yellow arrow), the basement membrane of renal tubules (blue arrow), the basement membrane of Bowman's capsule (red arrow), the basement membrane of atrophic renal tubule (white arrow), and Kimmelstiel-Wilson nodules (orange arrow). The lower panel is the quantification of $^{79}Br/^{13}C$ ratio for regions of interest (ROI) (mean ± SD) in the specimen from Patient 3. Glomerular basement membrane (BM), n = 53 ROIs; Bowman capsule BM, n = 32 ROIs; renal tubule BM, n = 65 ROIs; atrophic renal tubule BM, n = 10 ROIs; extracellular matrix between renal tubules (ECM), n = 59 ROIs; Kimmelstiel-Wilson nodules, n = 66 ROIs. Scale bars, 40 μm.

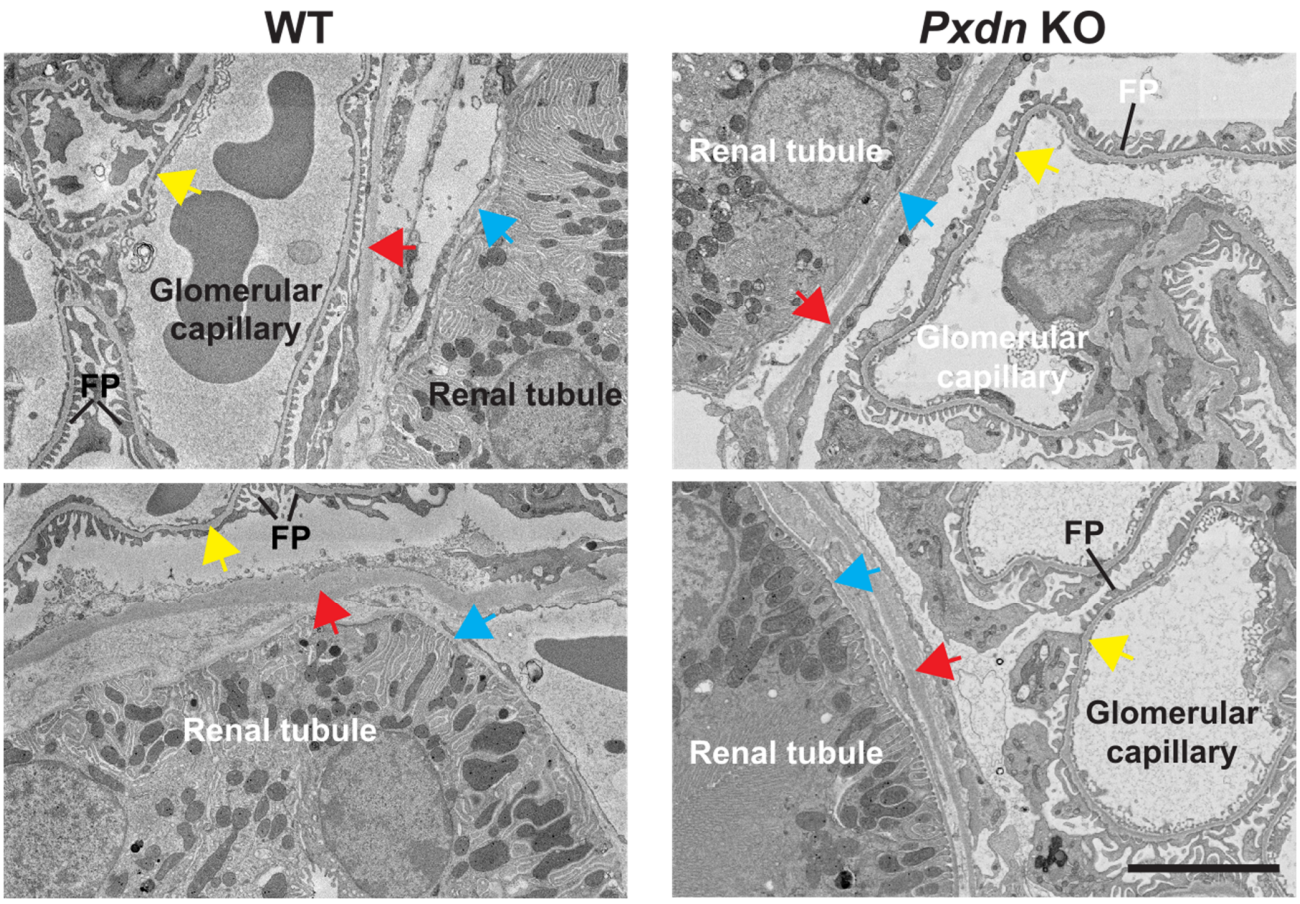

Fig. S10. Backscattered electron micrographs of two different regions of the kidney in wild-type and peroxidasin knockout (*Pxdn* KO) mice. Yellow arrows, glomerular basement membrane; blue arrows, renal tubule basement membrane; red arrows, Bowman's capsule basement membrane; FP, podocyte foot processes. Scale bars, 5 μm.

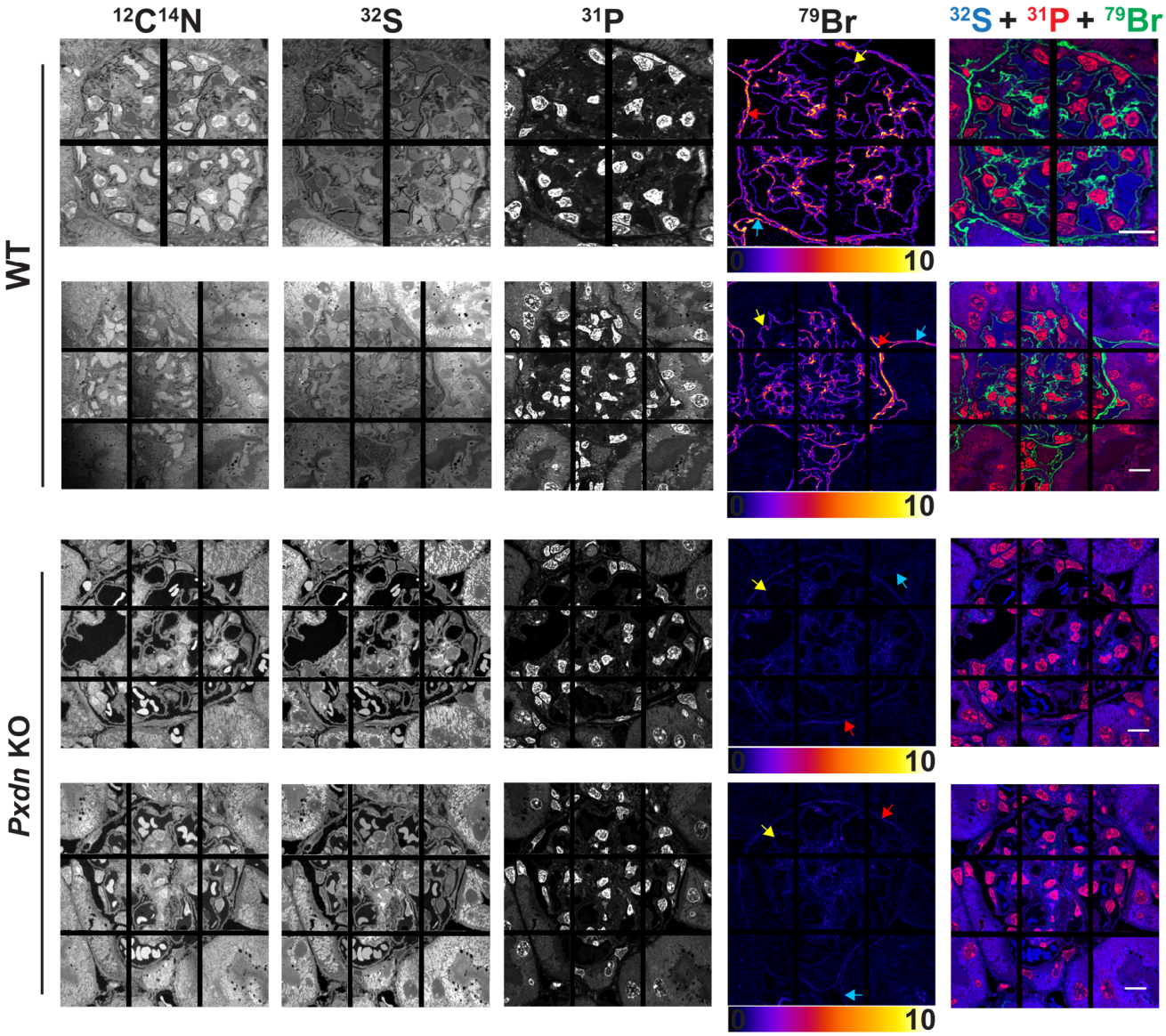

Fig. S11. NanoSIMS images of glomeruli from kidneys of wild-type (WT) and peroxidasin knockout (*Pxdn* KO) mice. $^{12}C^{14}N$, ^{31}P, and ^{32}S images were useful for visualizing tissue morphology. ^{79}Br and composite ^{31}P (red), ^{32}S (blue) and ^{79}Br (green) NanoSIMS images reveal bromine enrichment in the glomerular basement membrane (yellow arrows), the renal tubule basement membrane (blue arrows), and the basement membrane of Bowman's capsule (red arrows) in WT mice. Bromine levels were dramatically reduced in the *Pxdn* KO mice. The upper panels of the WT images and the upper panels of the *Pxdn* KO images show additional NanoSIMS images of the same glomeruli depicted in Fig. 6. The lower panels in the WT and *Pxdn* KO images show NanoSIMS images of another WT glomerulus and another *Pxdn* KO glomerulus. Scale bars, 10 μm.

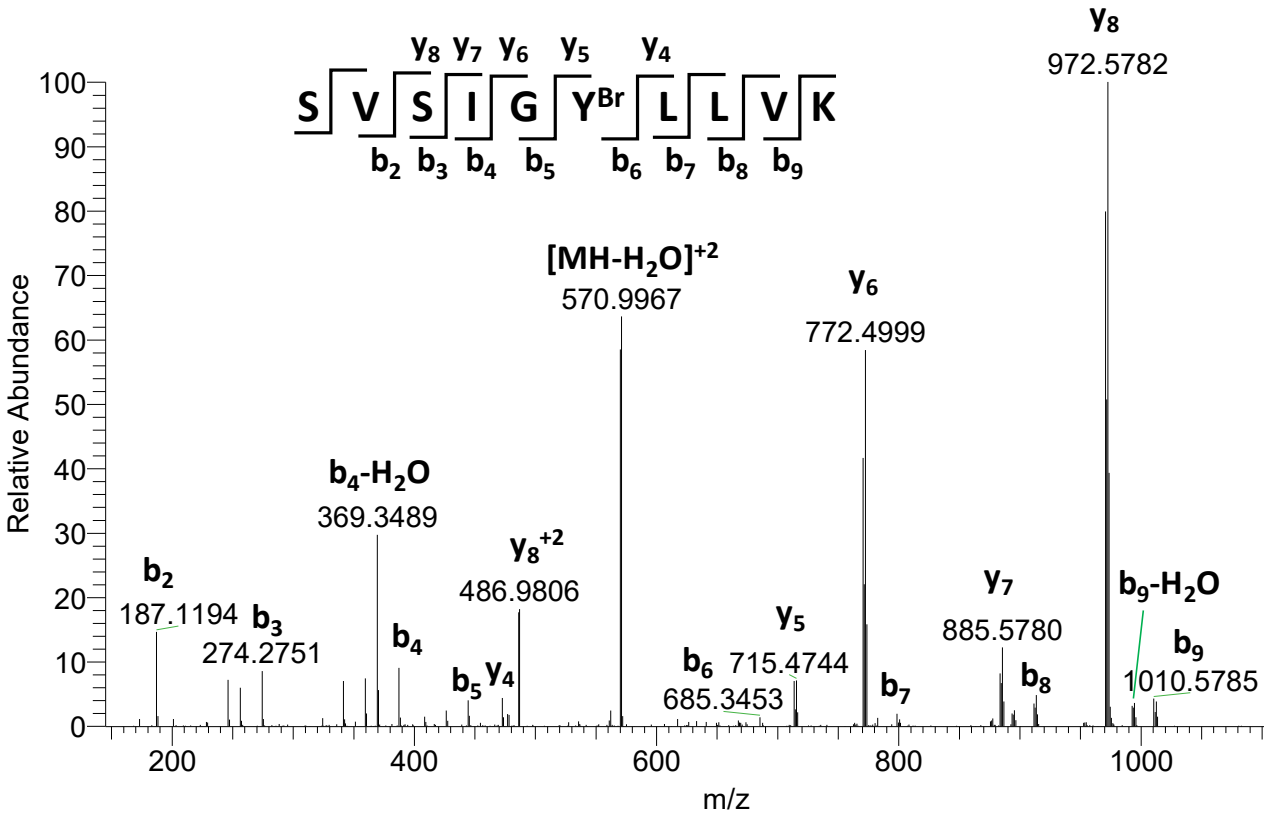

Fig. S12. Bromination site in the α2NC1 domain of collagen IV from human kidney. NC1 domains from collagen IV were isolated from human kidney tissue and analyzed by LC-MSMS as described in the *Materials and Methods*. Shown are MS^2 spectra of a brominated peptide from the α2NC1 domain, including peak assignments. *Inset* shows the sequence of brominated precursor peptide and the MS^2 fragmentation pattern producing specific y- and b-ions.

Table S1. Identification of brominated sites in the NC1 domains of collagen IV from mouse and human kidneys.

Protein	Peptide sequence [a]	Observed MH^{+2} precursor ion [b]	Mass accuracy (ppm)	Normalized relative abundance [c]	Site of modification
Mouse α2NC1(IV)	(R^{1479})SVSIG**Y^{Br}**LLVK(H^{1490}) (R^{1479})SVSIGYLLVK(H^{1490})	578.7822 539.8295	–3.5 0.9	(1.24 ± 0.17) × 10^{-2}	Y^{1485}
Human α2NC1(IV)	(R^{1484})SVSIG**Y^{Br}**LLVK(H^{1495}) (R^{1484})SVSIGYLLVK(H^{1495})	578.7833 539.8277	–1.6 –2.4	7.85 × 10^{-3}	Y^{1490}

[a] The amino acid positions are provided for full-length α2(IV) chain sequences (UniProtKB: P08122, CO4A2_MOUSE; P08572, CO4A2_HUMAN). Brominated tyrosine (Y^{Br}) residues are indicated in bold. [b] Values are measured at the maximum peak intensity. [c] Normalized relative abundance represents modified peptide / (modified peptide + unmodified peptide). The mouse data are expressed as means ± SD for three independent kidney NC1 preparations; the human data are from a single NC1 preparation from human kidney.